

LA-UR-15-28555 (Accepted Manuscript)

The origin of infrasonic ionosphere oscillations over tropospheric thunderstorms

Shao, Xuan-Min
Lay, Erin Hoffmann

Provided by the author(s) and the Los Alamos National Laboratory (2017-01-12).

To be published in: Journal of Geophysical Research: Space Physics

DOI to publisher's version: 10.1002/2015JA022118

Permalink to record: <http://permalink.lanl.gov/object/view?what=info:lanl-repo/lareport/LA-UR-15-28555>

Disclaimer:

Approved for public release. Los Alamos National Laboratory, an affirmative action/equal opportunity employer, is operated by the Los Alamos National Security, LLC for the National Nuclear Security Administration of the U.S. Department of Energy under contract DE-AC52-06NA25396. Los Alamos National Laboratory strongly supports academic freedom and a researcher's right to publish; as an institution, however, the Laboratory does not endorse the viewpoint of a publication or guarantee its technical correctness.

RESEARCH ARTICLE

10.1002/2015JA022118

Key Points:

- New technique to locate source of infrasonic wave by using phase difference of GPS-TEC measurements
- Sources located near thunderstorm core but more likely related to downdraft than to updraft
- Sources also located in stratiform region, related to lightning and sprites in and above the region

Correspondence to:

X.-M. Shao,
xshao@lanl.gov

Citation:

Shao, X.-M., and E. H. Lay (2016), The origin of infrasonic ionosphere oscillations over tropospheric thunderstorms, *J. Geophys. Res. Space Physics*, 121, doi:10.1002/2015JA022118.

Received 3 NOV 2015

Accepted 14 JUN 2016

Accepted article online 16 JUN 2016

The origin of infrasonic ionosphere oscillations over tropospheric thunderstorms

Xuan-Min Shao¹ and Erin H. Lay¹
¹Space and Remote Sensing Group, Los Alamos National Laboratory, Los Alamos, New Mexico, USA

Abstract Thunderstorms have been observed to introduce infrasonic oscillations in the ionosphere, but it is not clear what processes or which parts of the thunderstorm generate the oscillations. In this paper, we present a new technique that uses an array of ground-based GPS total electron content (TEC) measurements to locate the source of the infrasonic oscillations and compare the source locations with thunderstorm features to understand the possible source mechanisms. The location technique utilizes *instantaneous* phase differences between pairs of GPS-TEC measurements and an algorithm to best fit the measured and the expected phase differences for assumed source positions and other related parameters. In this preliminary study, the infrasound waves are assumed to propagate along simple geometric raypaths from the source to the measurement locations to avoid extensive computations. The located sources are compared in time and space with thunderstorm development and lightning activity. Sources are often found near the main storm cells, but they are more likely related to the downdraft process than to the updraft process. The sources are also commonly found in the convectively quiet stratiform regions behind active cells and are in good coincidence with extensive lightning discharges and inferred high-altitude sprites discharges.

1. Introduction

Since the 1960s, infrasonic oscillations in the ionosphere have been observed in relation to thunderstorms in the troposphere. The oscillations are typically sinusoidal in nature and have a relatively well-defined frequency range between 3 and 17 mHz (with corresponding time periods of 5 and 1 min), with most of the power in a narrower frequency band of 3–5 mHz. These infrasonic oscillations have been detected in the ionosphere's *F* region (200–400 km) [e.g., Georges, 1968; Baker and Davies, 1969; Davies and Jones, 1971, 1973; Georges, 1973; Prasad et al., 1975; Raju et al., 1981; Sindelarova et al., 2009; Lay et al., 2013, 2015; Nishioka et al., 2013] as well as in the *D* region (80–100 km) [Pilger et al., 2013; Marshall and Snively, 2014], indicating an extended upward infrasonic coupling from tropospheric thunderstorms into the ionosphere.

Most of the observed infrasonic oscillations were detected by examining the Doppler shift of radio signals reflected off the ionosphere with ground-based transmitters and receivers. Oscillations detected with this technique are sensitive to the variations of reflection height. For instance, high-frequency radio signals are used to probe the *F*-layer height oscillations [e.g., Baker and Davies, 1969] and very low frequency (VLF) radio signals are used to probe *D*-layer oscillations [Marshall and Snively, 2014].

By examining the total electron content (TEC) measurement from ground-based GPS receivers, Lay et al. [2013] found a case of similar thunderstorm-related infrasonic oscillations (in addition to atmospheric gravity wave variations) in the ionosphere. Following the case study, Lay et al. [2015] analyzed 3 months of continuous GPS-TEC measurement over an area of 1200 km × 1200 km in the U.S. Great Plains and compared the TEC measurements in space and time with thunderstorm activities observed by the National Weather Service's Next Generation Weather Radar (NEXRAD) network. This extended, statistical study showed unambiguously that the majority of the infrasonic oscillations in the ionosphere over the Great Plains were related to thunderstorms, with the exception of a few days in the entire 3 months, in which the oscillations were likely related to high geomagnetic activity. Different than radio reflection techniques, GPS-TEC measures the integrated electron density along the line of sight from ground GPS receivers to GPS satellites and the TEC oscillation is therefore more sensitive to the density variation than to the height variation in the ionosphere.

From these observations, it is clear that thunderstorms can produce detectable infrasonic oscillations in the ionosphere, and thunderstorms appear to be the dominant natural sources for such oscillations over the Great Plains. However, it is not clear what specific processes in the thunderstorm are responsible for the oscillations. Since the earliest findings, intense upward convection in thunderstorms has been considered

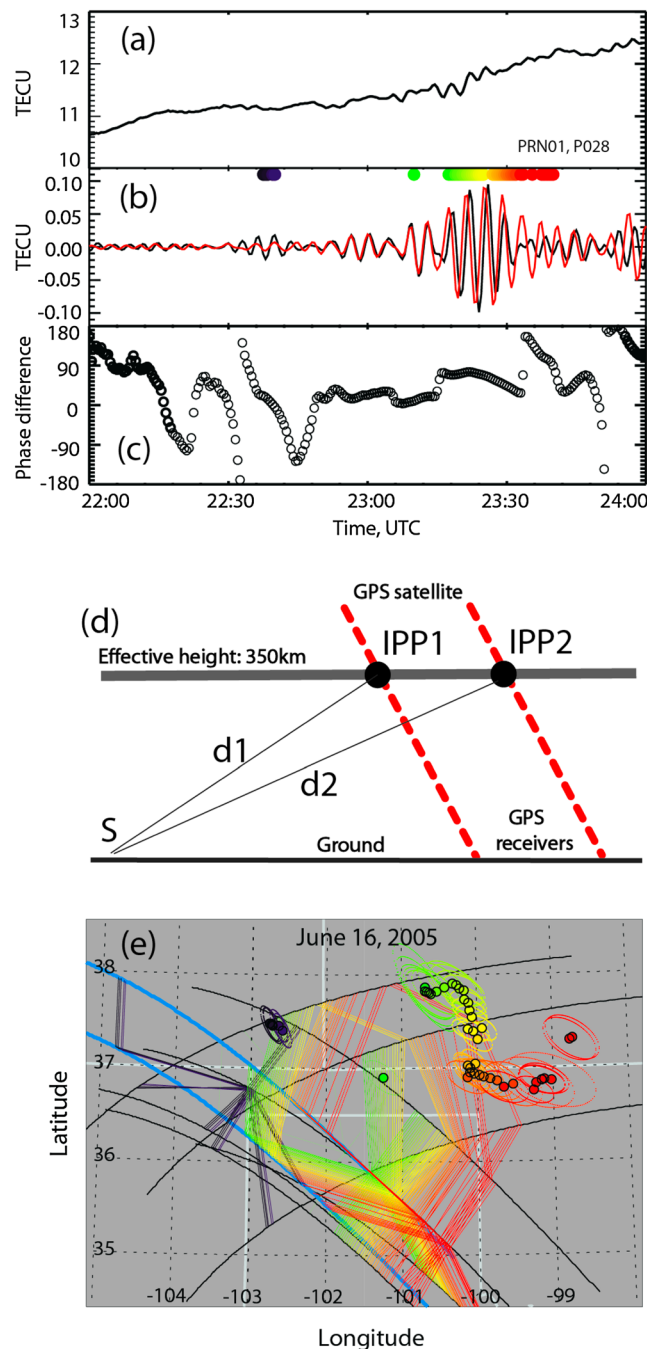


Figure 1. Illustration of GPS-TEC infrasonic oscillations and the concept of geolocation technique. (a) Example of raw TEC record. (b) TEC infrasonic oscillations after detrending and band-pass filtering of the raw TEC records. The black and red lines show measurements along the upper and lower blue tracks in Figure 1e. (c) Instantaneous phase difference between the two signals in Figure 1b. (d) Illustration of GPS-TEC measurements (red dashed lines), effective ionosphere height (thick gray line), IPPs (black circles), and infrasonic propagation paths (thin solid lines). (e) The long arcs show the IPP tracks for ten GPS-TEC measurements, the colored straight lines show the selected baselines for phase difference measurements, the black circles filled with colors show the located source positions, and the corresponding ellipses show the errors for the source positions. The colors in Figures 1b and 1e are synchronized to show the time sequence of the measurements.

as the source [e.g., *Georges, 1973*], but the causal relation has not been confirmed. The most direct comparison between the source of ionosphere oscillations and thunderstorms was reported by *Davies and Jones [1973]* by acoustic ray-tracing based on the horizontal propagation velocity of the *F* region oscillations. This comparison indicated the sources to be in the vicinity of thunderstorms but could not relate the sources to specific regions or processes of the storms, apparently due to the quality of the radar observations of thunderstorms at the time. Recent modeling studies [*Walterscheid et al., 2003; Zettergren and Snively, 2013, 2015; Snively, 2013*] have simulated a convection process in the upper portion of the storms with an energy disturbance in the upper troposphere on the order of minutes duration and have shown that the resultant infrasonic signals can propagate to ionospheric heights.

To understand the source-effect causal relation and to examine the model simulation, it is necessary to connect the ionospheric oscillations to specific regions/processes in the storms. In this paper, we present a new technique to locate the origins of the infrasonic oscillations based on differential phases among an array of GPS-TEC measurements. The source locations are then compared to time-resolved, three-dimensional thunderstorm features observed by NEXRAD and lightning activity observed by the National Lightning Detection Network (NLDN) and Oklahoma Lightning Mapping Array (OK-LMA) to examine the corresponding thunderstorm processes that might be responsible for the ionospheric oscillations.

2. TEC Data Preparation

The process for extracting the infrasonic signal from raw GPS-TEC data has been described previously in detail in *Lay et al. [2013, 2015]*. This process is demonstrated in Figures 1a and 1b for a 2 h TEC record. We first detrend the raw TEC record (Figure 1a) by subtracting its sixth-order polynomial fit to

remove the offset and the slow background TEC changes. The detrended record is then band-pass filtered in the frequency range of 3–5 mHz (3–5 min in time period) to retain the infrasonic oscillations (black curve in Figure 1b). In this case, the peak-to-peak infrasonic oscillation magnitude reaches 0.2 total electron content unit (TECU) ($1 \text{ TECU} = 10^{16} \text{ el m}^{-2}$) near 23:20 UTC, about 2% of the background TEC value.

As in *Lay et al.* [2013, 2015], the TEC measurements in this study (e.g., Figures 1a and 1b) have been converted to vertical TEC (VTEC) based on the satellite elevation angle viewed from the ground GPS receiver and the effective height of the ionosphere (350 km) [Seemala and Valladares, 2011]. The VTEC measurement at any given time is tagged with the corresponding position (latitude and longitude) of the ionosphere's pierce point (IPP). The IPP is defined as the location where the receiver-satellite path intercepts a given ionosphere height, as illustrated in Figure 1d by the red dotted lines and the effective ionosphere layer. An ionospheric height of 350 km was used in this study. The long arcs in Figure 1e show the IPP traces for 10 receiver-satellite line of sight during a 2 h time period while the GPS satellites move across the sky.

3. Locating the Infrasonic Source With GPS-TEC Phase-Difference Measurements

Figure 1b shows the infrasonic TEC variations measured by two closely spaced GPS receivers during a 2 h time period while the GPS satellite progresses across the sky. As expected, it is impossible to link these oscillations affirmatively to any specific sources by examining only one or a few of such records. Fortunately, the Continuously Operating Reference Station (CORS; <http://geodesy.noaa.gov/CORS/>) GPS network operated by the National Oceanic and Atmospheric Administration has many tens of ground GPS receivers in the U.S. Great Plains. Measurements from such an array offer a possibility to locate the sources. For an impulsive and isolated disturbance, one could use the differences of time of arrival (DTOA) among an array of measurements to geolocate the source [Park et al., 2011]. For continuous sinusoidal oscillations, as shown in Figure 1b, it is difficult to time-correlate a specific part of the record from one measurement to the other, and the DTOA approach is not feasible.

Here we present a new technique that utilizes the instantaneous phase differences among an array of GPS-TEC measurements. The red dotted lines in Figure 1d illustrate a pair of spatially separated TEC measurements, and the black dots show their IPPs. The two IPPs form a vector in space that is used as a baseline for the phase difference measurement. The phase difference for a continuous wave is related to path difference from the source to the IPPs in the ionosphere. However, due to the continuous movement of the GPS satellite, the baseline vector changes continuously with time, such that the corresponding phase difference will change accordingly with time for a stationary source. In addition, for IPPs within a few hundred kilometers (comparable to the infrasound wavelength in the ionosphere) of a localized source the wave cannot be treated as a plane wave. These make it difficult to apply the conventional interferometry technique to determine the direction of the source. Nevertheless, in the case that the wave might be assumed to be a plane wave, Gómez et al. [2015] developed a beamforming technique to compensate the convolved phase changes due to the time-evolving geometric changes of the IPPs and were able to determine the direction of the infrasound wave.

In this study, we measure the *instantaneous* phase difference at each time instant (each 30 s, the CORS TEC sampling rate) for the specific baseline vector at the time. The instantaneous phase $\phi(t_i)$ for each record is computed by $\phi(t_i) = \tan^{-1}[H(s(t_i))/s(t_i)]$, where $s(t_i)$ is the original data record and $H(s(t_i))$ is the Hilbert transformation of the original record. The instantaneous phase difference for the corresponding baseline is obtained by $d\phi_{21}(t_i) = \phi_2(t_i) - \phi_1(t_i)$. In Figure 1b, the black curve shows a 2 h infrasonic TEC measurement from one GPS receiver while its corresponding IPPs progress from $(-105^\circ, 38^\circ)$ toward southeast (the upper blue track in Figure 1e), and the red curve in Figure 1b shows a similar measurement by another GPS receiver along the lower blue track in Figure 1e. Figure 1c shows the instantaneous phase differences at each data point between the two measurements.

If there are enough spatially diversified baselines at a given time instant, and if the infrasonic wave is detected by enough number of the baselines, it is possible to use the corresponding phase differences to determine the source location at the specific time instant. To explore this idea, we assume simply that the infrasound wave travels along geometric raypaths from the source to the IPPs (Figure 1d), same as that assumed in Park et al. [2011]. This assumption is reasonable for nearby (a few hundred kilometer) GPS-TEC

observations of a localized source because the wave propagating into the ionosphere can be approximated by a spherical wave, as modeled by *Walterscheid et al.* [2003] and *Zettergren and Snively* [2015]. With this assumption, the phase velocity (an effective velocity) will be assumed to be constant from the source to the IPPs along the raypath. More realistic and thorough treatment of the wave propagation could be realized by using infrasound ray-tracing or full-wave calculations from all the possible source locations to all the disturbed regions in the ionosphere with considerations of more realistic infrasound velocity and wind field profiles from ground to the ionosphere. Although feasible, the more thorough treatment would require extensive computations and will be attempted in the future.

With the geometric raypath approach, we assume that the phase path lengths are d_1 and d_2 (Figure 1d), the phase difference between the two IPPs can be expressed as

$$d\phi_{21} = 2\pi \frac{d_2 - d_1}{\lambda} = 2\pi \frac{d_2 - d_1}{vT} \quad (1)$$

where λ is the effective wavelength of the infrasonic wave, v is the effective infrasonic phase velocity, T is the time period of the signal (4 min in this study), and d_1 and d_2 are related to the source location (ϕ_s, θ_s, h_s) and the IPP locations (ϕ_1, θ_1, h_i) and (ϕ_2, θ_2, h_i) . Here ϕ and θ stand for the longitude and latitude, h_s is the source height, and $h_i = 350$ km is the effective ionosphere height. To account for the spherical curvature of the Earth and the ionosphere, we approximate the path length from the source to the i th IPP by $d_i = \sqrt{(h_i - h_s)^2 + l_i^2}$ where $h_i = 350$ km and l_i is the spherical arc-length at 350 km altitude between (ϕ_s, θ_s, h_i) and (ϕ_i, θ_i, h_i) . Based on these assumptions, there are four independent unknown source parameters $(\phi_s, \theta_s, h_s, v)$ involved in equation (1). To determine the four source parameters, four or more IPP baseline measurements are needed.

In this study, the values of the four parameters are determined by a least χ^2 fit between the measured phase differences and the estimated phase differences for a set of assumed source parameters. The reduced χ^2 is computed as

$$\chi_m^2 = \frac{1}{m} \sum_{n=1}^N \frac{([d\phi]_{\text{measured}} - [d\phi]_{\text{estimated}})_n^2}{\sigma_n^2} \quad (2)$$

where N is the total number of baselines, $m = N - 4$ is the degrees of freedom; and σ_n is the phase error related to the n th baseline measurement.

Two main factors are considered to contribute to the phase error in the current study: (1) the finite digitization rate of the GPS-TEC data and (2) the signal-to-noise ratio (SNR) of the TEC measurement. In this study, the TEC data of CORS network are sampled every 30 s, and the infrasound signal is centered at 4 min time period. So the phase error due to the digitization can be estimated by $\sigma_{\text{digit}} = 2\pi / (8\sqrt{12})$ [Oppenheim and Schaffer, 1999, page 196]. Due to the finite bandwidth (4 ± 1 min), this phase error can be further increased to $\sigma_{\text{digit}} = 2\pi / ((8\sqrt{12})(1 - 0.125)) = 0.26$ radians (or 14.9°). The error of the phase difference related to SNR follows a Gaussian distribution with $\sigma_{\text{SNR}} = \sigma_{\text{rms}} / \sqrt{A_1 A_2}$ [Thompson et al., 2001, page 193], where σ_{rms} is the noise level for the infrasonic TEC data record (e.g., noise level in Figure 1b) and A_1 and A_2 are the instantaneous signal amplitudes measured by the two receivers that form the specific baseline. GPS-TEC measurements are accurate to 0.01–0.1 TECU [Burrell et al., 2009], and we assume $\sigma_{\text{rms}} = 0.03$ TECU for the infrasonic frequencies in this study. Since the errors related to digitization and SNR are independent of each other, σ_n^2 in equation (2) can be expressed as $\sigma_n^2 = \sigma_{\text{digit}}^2 + \sigma_{\text{SNR}}^2$.

There are other possible error sources that are not included in the current study. First, the background wind field from the ground to the ionosphere would affect the infrasound propagation speed and direction. Horizontal wind profile based on the empirical model HWM07 [Drob et al., 2008] suggests a maximum wind speed of 40–60 m/s from the ground to the ionosphere over the time and area for this study, which corresponds to about 13% and 4% of the infrasound propagation speed in the troposphere and ionosphere. To take this into account, a thorough ray-tracing or full-wave treatment of the infrasound propagation is needed. Nevertheless, since our IPPs and baselines are typically situated in a variety of different horizontal directions to the source (Figure 1e), and since the source position will be best fitted with these directionally diversified measurements, the effect of the horizontal wind on our fitted source position would be minimized.

The other source of error might be due to the ionospheric plasma coupling to the neutral wave [Georges and Hooke, 1970; Gómez *et al.*, 2015]. However, for a typical observational geometry in this study and by using the equations in Georges and Hooke [1970] and Gómez *et al.* [2015] a small phase offset of 1–3° between two IPPs was estimated. Furthermore, recent observations [Nishioka *et al.*, 2013] and more realistic simulations [Zettergren and Snively, 2015] for infrasonic TEC oscillations in the low-latitude and midlatitude regions do not show detectable phase offset related to this effect.

To use the phase difference technique, we need to consider possible phase ambiguity effects. For a baseline that is longer than a wavelength, the actual phase difference could be greater than 2π if the wave propagates along the baseline from one IPP to the next. However, the measureable phase difference is limited in a 2π range (Figure 1c). To avoid this possible ambiguity, the baseline must be shorter than the infrasonic wavelength. The propagation speed of infrasound in the ionosphere's *F* region is about 1 km/s [e.g., Davies and Jones, 1973; Nishioka *et al.*, 2013; Zettergren and Snively, 2015]. For signals in the 3–5 min time period, the corresponding wavelengths are about 180–300 km. In this study we limit the baselines to be shorter than 200 km by selecting the proper pairs among the spatially distributed measurements. The long arcs (black and blue) in Figure 1e show the IPP tracks for 10 GPS-TEC measurements during 22:00–24:00 UTC on 16 June 2005. The seven arcs that progress from northwest to southeast are associated with seven GPS receivers (nmsf, p036, p034, p035, azcn, p028, and zab2) tracking the same satellite PRN01, and the three arcs from southwest to northeast are associated with three receivers (nmro, p035, and p034) tracking another satellite PRN25. At each time instant (30 s apart), up to nine baselines are selected among the ten IPPs and the four source parameters at the corresponding time instant are estimated by minimizing equation (2). The thin colored straight lines in Figure 1e that connect the IPP tracks show the selected baselines as the IPPs progress across the ionosphere. The colors for the baselines indicate the time sequence, as correspondingly shown at the top of Figure 1b. Figure 1e shows only the baselines at the times when “good” source locations are found but not all the baselines during the 2 h time period, as will be further discussed.

The black circles in Figure 1e show the ground projection of the source locations (longitudes and latitudes) for those that are successfully located by the technique. The circles are filled with the same sequence of colors to indicate the time of the sources (Figure 1b) and to associate with the baselines (Figure 1e) that are used for the geolocation. The small oscillations seen in Figure 1b just past 22:30 UTC (black) are located in an area near (−102.8°, 37.5°) in Figure 1e, and the oscillations between 23:15 to 23:45 UTC (green to red in Figures 1b and 1e) are associated with a much more extended source region. The oscillations between 22:40 and 23:15 UTC in Figure 1b were not successfully located by this technique, probably due to strong interferences among multiple sources.

To examine the errors associated with the best fitted source parameters (ϕ_s , θ_s , h_s , and v), we compute the 4×4 error matrix that estimates the variance for each fitted parameter and the co-variance for each pair of the parameters [Bevington and Robinson, 1992]. Figures 2a–2d show the values of the four fitted parameters and their variances for the selected good sources (Figure 1e). The black dots in each plot are the best fitted values, and the colored vertical lines show the corresponding variances. The same time sequence of colors is used here as that in Figures 1b and 1e for the purpose of comparison.

The heights for many sources are fitted to some large, nonphysical negative values (hundreds of kilometers below ground), and some (near and after 23:30 UTC) even to negative thousands of kilometers that are off the plot scale. This can be explained by the nature of the infrasound propagation from the troposphere to the ionosphere. For IPPs that are far from the source, the wave would be viewed to propagate dominantly horizontally as if the source was high in the ionosphere. For IPPs that are vertically above the source, the source would be viewed to be nearly infinitely far under the IPPs, due to a flatter wavefront in the vertical direction. Therefore, the source height determined by this technique depends on the positions of the baselines and can only be considered as a “virtual” height. For instance, when all the baselines are far from the source (greater than ~200 km in horizontal distance, the green baselines in Figure 1e), the source heights are determined to be in the ionosphere (around 200 km altitude; Figure 2c). As some of the baselines move closer to the top of the source, the virtual height starts to decrease (e.g., green to yellow in Figures 1e and 2c) and may even become negative values (yellow to red in Figures 1e and 2c).

The fitted propagation velocity changes accordingly with the source height. For the sources marked with the green colors the velocity was determined to be around 1 km/s (Figure 2d), in good agreement with

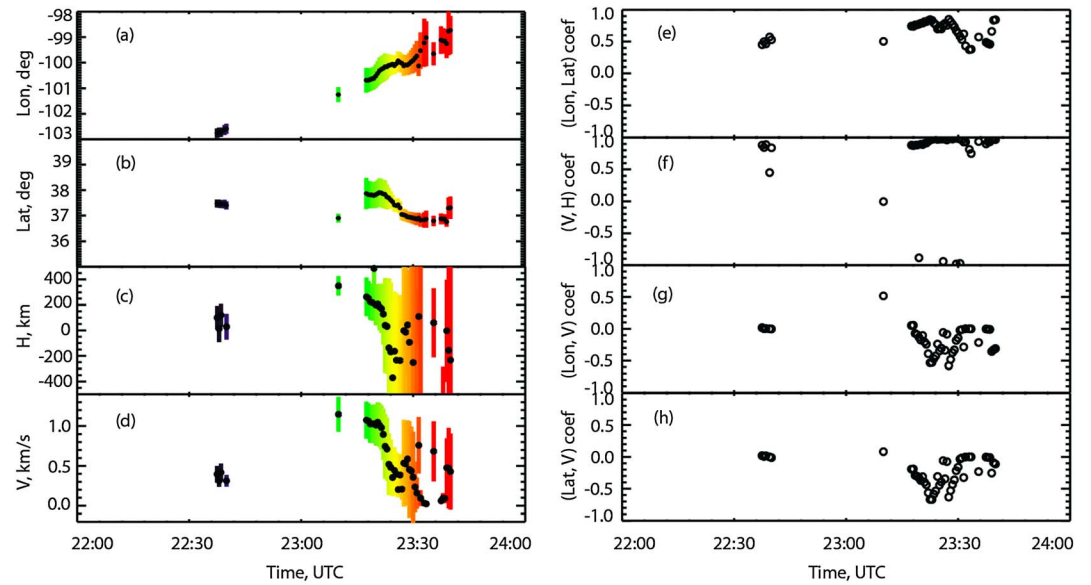


Figure 2. (a–d) Black dots: best fitted source longitude, latitude, height, and propagation speed, respectively. Colored bars: variance for the best fitted parameters. The colors are synchronized with those in Figure 1. (e–h): Correlation coefficients between four chosen pairs of the best fitted parameters.

infrasound phase velocity in the ionosphere. For sources with lower virtual heights (baselines closer to directly above the source) the velocity decreases, as the velocity is more determined by the troposphere-mesosphere infrasound velocity (~ 0.3 km/s).

The behavior of the height and velocity leads us to examine the cross correlations among the four fitted source parameters (ϕ_s , θ_s , h_s , and v). Figures 2e–2h show the correlation coefficients for four of the total of six pairs based on $c_{ij} = \sigma_{ij}^2 / \sigma_i \sigma_j$, where σ_{ij} is the covariance between the i th and the j th parameters and σ_i and σ_j are the variances for the two parameters. Figure 2f shows that the correlation coefficients for (h_s , v) are high (close to ± 1) for most of the selected sources. The high coefficients indicate that to vary h_s near the minimum χ_m^2 (equation (2)), the value for v has to be adjusted accordingly to maintain the minimum χ_m^2 . The high correlation coefficients for this pair explain the similar behavior in Figures 2c and 2d. Figure 2e shows that the correlation between ϕ_s and θ_s , the horizontal position of the source, are high as well (mostly above 0.5), showing that a proper pair of (ϕ_s , θ_s) needs to be found to best fit the measurements. On the other hand, correlations for (ϕ_s , v) and (θ_s , v) are relatively weak (Figures 2g and 2h), mostly within $|\pm 0.6|$. Similar weak correlations are found for (ϕ_s , h) and (θ_s , h) and are not shown here. These weak correlations indicate that the fitted horizontal position (ϕ_s , θ_s) is less sensitive to the fitted velocity and height. Therefore, a good two-dimensional horizontal source position might be viable even if the height and velocity are not entirely physical.

In this study, to select a good located source, we require (1) $\chi_m^2 < 2$, (2) the mean of the signal amplitudes $\sqrt{A_i A_m}$ over all the participating baselines to be greater than 0.01 TECU, and (3) the half major axis of the error ellipse in (ϕ_s , θ_s) plane to be less than 0.7° . The error ellipse for each source location is computed from the variances and covariance of ϕ_s and θ_s , which indicate that the source has a 68% of probability to be within the ellipse for the best fit h_s and v .

4. Comparison of Source Locations With Thunderstorm Activity

NEXRAD provides thunderstorm observations across the continental U.S. and provides a complete 3-D volumetric scan of the storms every 5 min. Figure 3 overlays the infrasound source positions (longitudes, latitudes; white circles in the plots) for the time period of 23:15–23:45 UTC (Figure 1) on the horizontal cross sections of the radar reflectivity measurement. The strength of the radar reflectivity, which is related to the intensity of the storm, is represented by the colored contours, in a range from 0 to 60 dBZ. The height for the horizontal cross sections is chosen to be 7 km above the ground.

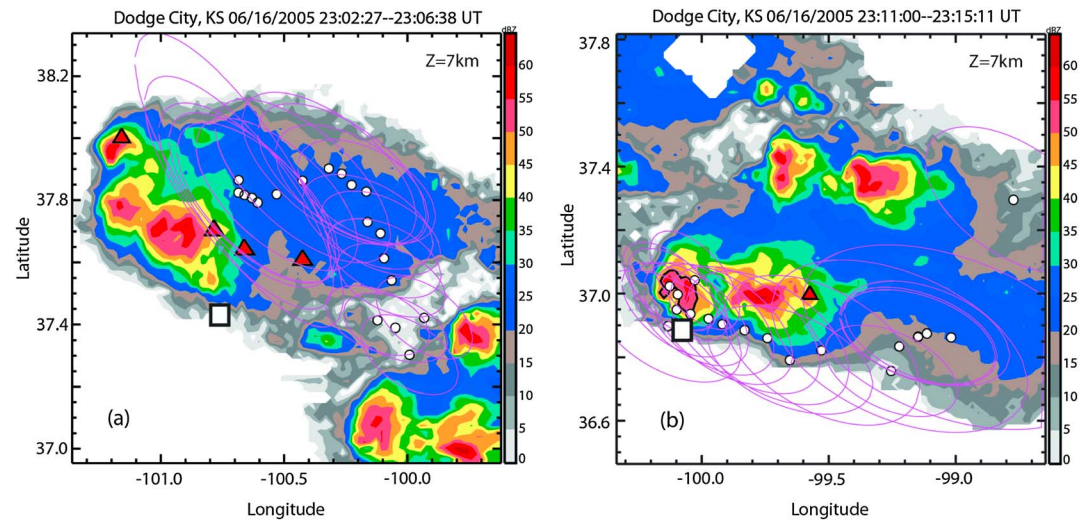


Figure 3. Overlay of the located infrasound sources (white circles) with NEXRAD radar reflectivity at 7 km altitude (filled colored contours). The magenta ellipses show error estimates for locations. (a) For the oscillation time interval of 23:15–23:25 UTC of Figure 1, radar reflectivity was chosen 10–15 min prior to the infrasound oscillation (23:02–23:06) to account for the infrasound propagation time from troposphere to the ionosphere. The red triangles show +CGs with peak current greater than 70 kA at the expected source time. The white square shows a tornado location that occurred ~40 min later. (b) Same as Figure 3a but for the time interval of 23:25–23:45 UTC. The white square marks a tornado that occurred at 23:25 UTC, about 10–15 min later than the estimated infrasound source time.

Figure 3a compares the first group of the extended sources during 23:15–23:25 UTC (from green to yellow colors in Figure 1) with the radar reflectivity obtained in a 5 min interval between 23:02 and 23:07 UTC. We choose the radar observation at this earlier time to account for the infrasonic propagation time of 10–15 min from the troposphere to the ionosphere. To our surprise, this group of infrasound sources is coincident with the stratiform region of the storm, which commonly has weak convection. This appears to suggest that these sources are not related to the convective activity of the storm, contrary to our expectations.

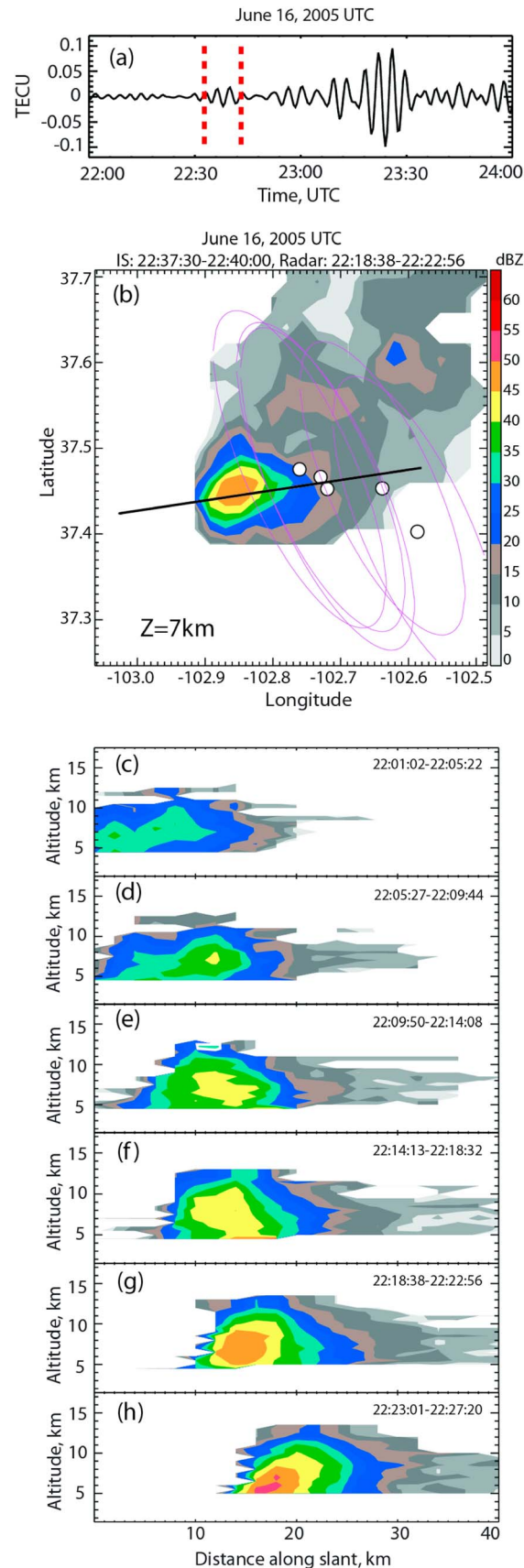
On the other hand, the next group of sources during 23:25–23:45 UTC (from orange to red colors in Figure 1) is mostly associated with intense convective cells, as shown in Figure 3b. To highlight the intensity of the left-most storm cell, a black contour is used to enclose the region in which the reflectivity is greater than 50 dBZ. The sources around this intense storm cell are apparently related to the intense convection, as would have been expected. Although the position errors (purple ellipses in the plots) are too large to compare the sources to the storm structure in more detail, it is intriguing to note that a number of the sources are positioned along the edge of the storm.

It should be noted that although the source positions appear to progress in time (Figure 1e), it is not necessarily true that the sources actually do so. For instance, for a spatially extended but temporally impulsive source, the signal from the source nearest to the measurements will arrive earliest in time and the signal from the farthest will arrive later, due to the finite infrasound propagation speed (~300 m/s in the upper troposphere). This delay in arrival time for a spatially extended but temporally instantaneous source could appear as a temporally progressing source.

Figure 3 suggests that there are at least two different regions in the thunderstorm that are responsible for the ionospheric infrasound oscillations. We have analyzed 5 days of GPS-TEC data and found in these case studies that the infrasound sources were related both to strong convective cells and to convectively quiet stratiform regions. In the following, we present some examples with more detailed analysis.

4.1. Infrasonic Sources Near Storm's Convection Core

To understand the relationship between sources and convective thunderstorm cells, we start with the group of localized sources in Figure 1 that were detected around 22:35 UTC. As shown in Figure 4, these sources are found to be associated with a small (about 10 km wide), short-lasting (<1 h life time), isolated storm. Figure 4a is a replica of the black curve in Figure 1b that shows TEC variations for the selected sources for this storm

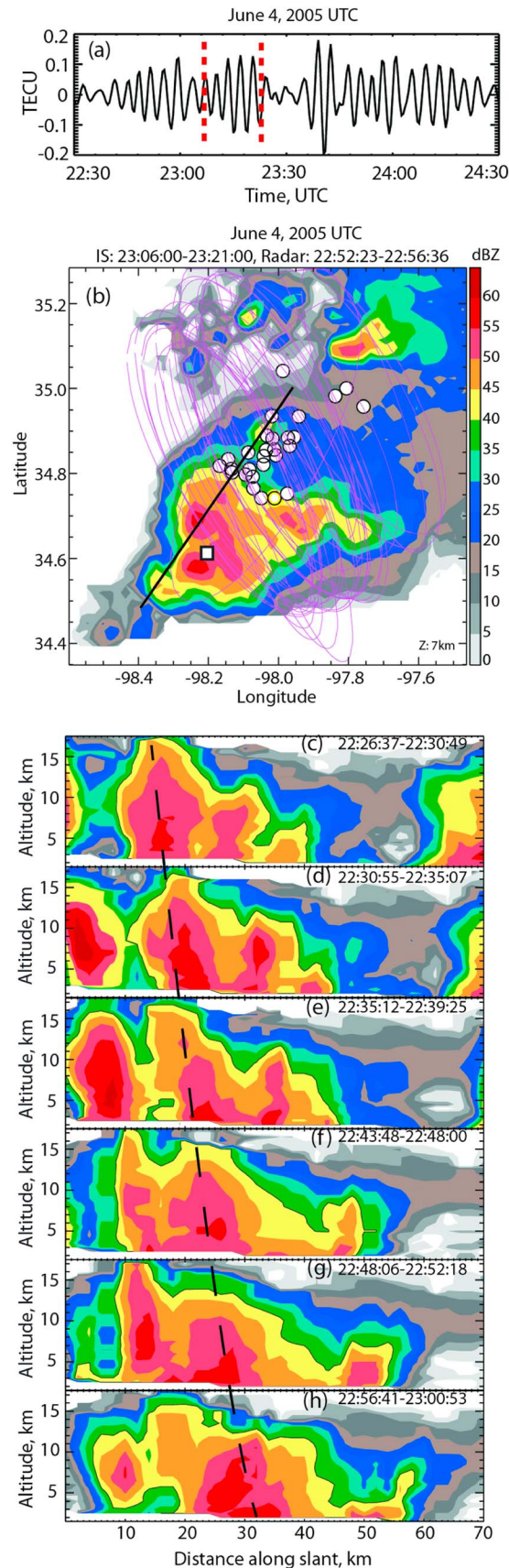


(between the red dashed lines) The sources were located next to and behind the convective core of the storm, as shown in Figure 4b. Taking into account of 10–15 min infrasonic propagation time from the troposphere to the corresponding IPPs in the ionosphere, the responsible sources are expected to occur at about 22:20–22:25 UTC.

Figures 4c–4h show a sequence of vertical radar cross sections sliced through the most intense reflectivity region of the storm to examine its vertical development prior to and near the time of the infrasonic sources. The black line in Figure 4a shows the location of this vertical slice on the horizontal plane. From 22:01 to 22:14 UTC (Figures 4c–4e) the storm was at its cumulus stage that continuously developed upward and appeared to overshoot the tropopause (~12 km altitude) by 22:14 (Figure 4e). After that, the storm reached its mature stage with a strong precipitation core (>45 dBZ) and the core started to descend (Figures 4f–4h). During the mature stage, the cloud top is expected to remain tall above the tropopause due to the sustained strong updraft in the upper part of the storm, as shown by the minimum detectable reflectivity (5 dBZ) in Figures 4f–4h. The descending of the precipitation core in Figures 4f–4g is due to either a weakening updraft below the core or the growth of the hydrometeor size in the core, as shown by *Kingsmill and Wakimoto* [1991] who studied a very similar storm in a great detail with simultaneous four-Doppler radar observations.

Comparing the estimated infrasonic source time with the radar observation sequence, the sources are found to be related to the mature stage of the storm, specifically to that in Figures 4g and 4h. This result is consistent with the hypothesis that the thunderstorm-related ionospheric infrasonic oscillations are associated with the storm's intense convection. However, it is noticed in Figure 4b that the sources are system-

Figure 4. Comparison of infrasound sources and the development of a small, isolated storm. (a) TEC oscillations in a 2 h time period. Oscillations between the red dashed lines are related to this storm. (b) Horizontal overlay of the sources (white circles with magenta error ellipses) and the radar reflectivity (filled colored contours). (c–h) Sequence of vertical radar cross sections sliced from left to right through the black straight line in Figure 4b. Infrasound sources are related to the mature stage of the storm shown in Figures 4g and 4h, but not related to the upward development stage in earlier times.

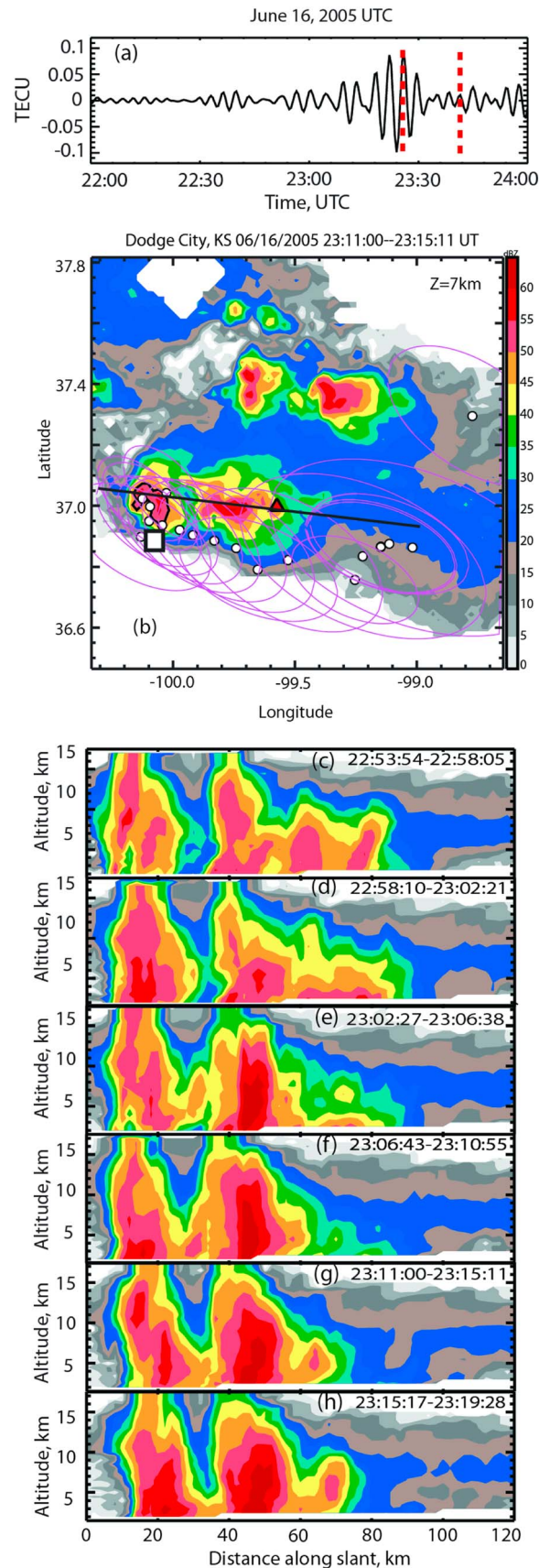


atically located behind the convection core away from the tallest part of the cloud. This could be due to the source location errors or may otherwise suggest a different source mechanism. Although NEXRAD does not provide enough information to reveal the full dynamics of the storm, the four-Doppler radar observation and the corresponding detailed analysis of a similar storm in *Kingsmill and Wakimoto* [1991] show an intense (>12 m/s) midlevel (6–12 km altitude) downdraft region just behind the intense updraft core during the mature stage of the storm. In their storm, the midlevel downdraft (MLD) was sustained for about 3–5 min. In fact, MLD is observed to be a common and important feature in thunderstorm development and is observed to occur at the proximity of the updraft core or at the edge of the cloud and is also called cloud-edge downdraft [e.g., *Knupp*, 1987]. If our storm in Figure 4 behaves similarly to that of the *Kingsmill and Wakimoto*'s, it is worthy to point out the apparent coincidence in space and time between MLD and the infrasound source, suggesting that the ionospheric infrasound in this case is more likely originated from the MLD than from the upward convection core.

Figure 5 shows the infrasound signal (Figure 5a) and the source locations (Figure 5b) related to a tornadic supercell thunderstorm that occurred on 4 June 2005 near Marlow, Oklahoma. Figure 5a shows a 2 h record of ionospheric TEC oscillations during which time the selected IPPs progress over the storms. The infrasound sources for the oscillations between the two dotted red lines from 23:06 to 23:21 are shown in Figure 5b. Sources for the oscillation burst prior to 23:00 were located at the southeast edge of the smaller cell at the upper right corner of the plot (not shown).

This supercell is one of the major storm cells along an extended line of storms that span from Texas to Nebraska, a typical mesoscale system in

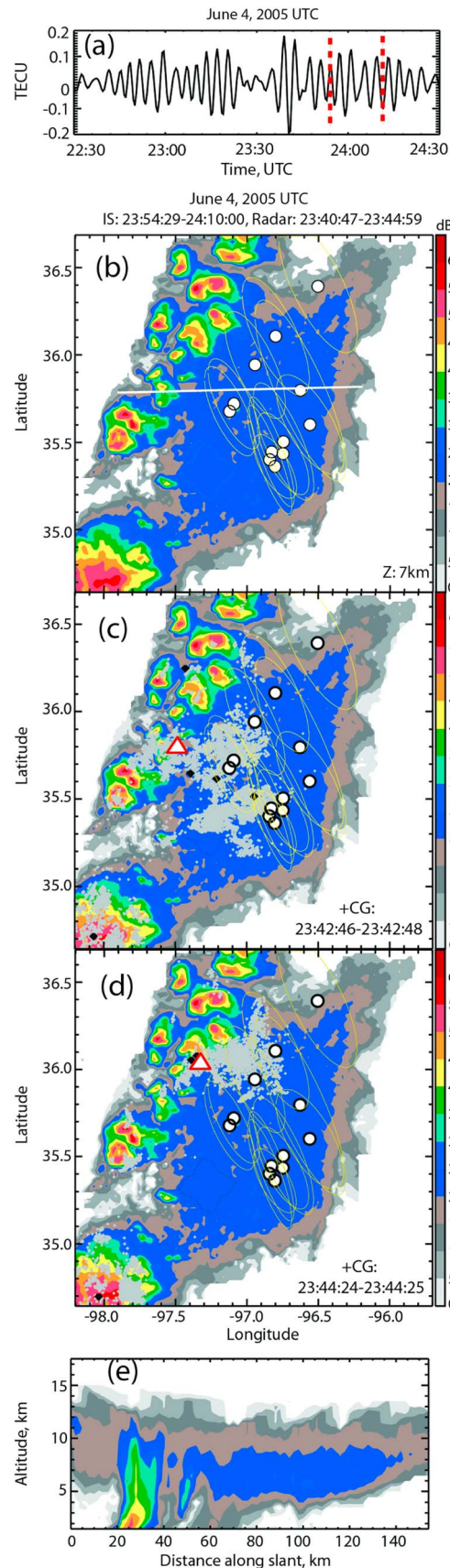
Figure 5. Infrasound sources related to a tornadic supercell. (a) A 2 h ionospheric TEC record shows the oscillations while the GPS-TEC measurements progress near the storm. (b) Overlay of the source positions during the time between the dashed red lines in Figure 5a and the radar reflectivity. The white square marks the tornado that occurred at 22:57 UTC. (c–h) Sequence of vertical radar reflectivity cross section sliced from lower left to upper right along the black line in Figure 5b, showing the vertical development of the supercell. The black dashed line tracks the main cell. The time for the sources is expected to be between that of Figures 5g and 5h, while the precipitation core is descending.



the U.S. Great Plains (<http://gis.ncdc.noaa.gov/map/viewer/#app=cdo&cfg=radar&theme=radar&display=nexrad>). The supercell spawned a tornado at $(-98.2^{\circ}, 34.6^{\circ})$ at 22:57 UTC, as marked by the white square in Figure 5b (http://www.spc.noaa.gov/climo/reports/050604_rpts.html). Figure 5b overlays the source positions on the horizontal cross section of the radar reflectivity at 7 km altitude at the time of the tornado, which is coincident temporally with the occurrence of the infrasound sources, about 10–15 min prior to the start of the TEC oscillation burst in the ionosphere. It is interesting to see that the sources are located behind the tornado and the intense precipitation/convection core of the storm. Although the location errors (purple ellipses) are large, it is interesting to note that many of the sources were located along the edge of the 45 dBZ radar reflectivity contour, similar to the features observed in Figure 3b that show the sources tend to follow preferred reflectivity contours near the edge of the storm. The rest of the sources in Figure 5b extend from the back of the core and are coincident with a weaker reflectivity region. For a well-developed tornadic supercell storm, a major midlevel downdraft region exists behind the main updraft core and is named forward flank downdraft (FFD) [e.g., Lemon and Doswell, 1979]. The infrasound source positions in Figure 5b are in coincidence with this FFD region, similar to the infrasound source/MLD region coincidence found in the small storm in Figure 4.

Figures 5c–5h show a selected time sequence of the vertical cross sections sliced along the black line in Figure 5b, during the time prior to and near the time of the detected ionospheric infrasound oscillations. The dashed line across Figures 5c–5h tracks the same main storm cell through its development. As shown by the vertical cross sections, this supercell was so intense that its cloud top overshoot the tropopause (~ 12 km) and reached above 18 km (the vertical limit of NEXRAD measurements) more than 30 min before the detection

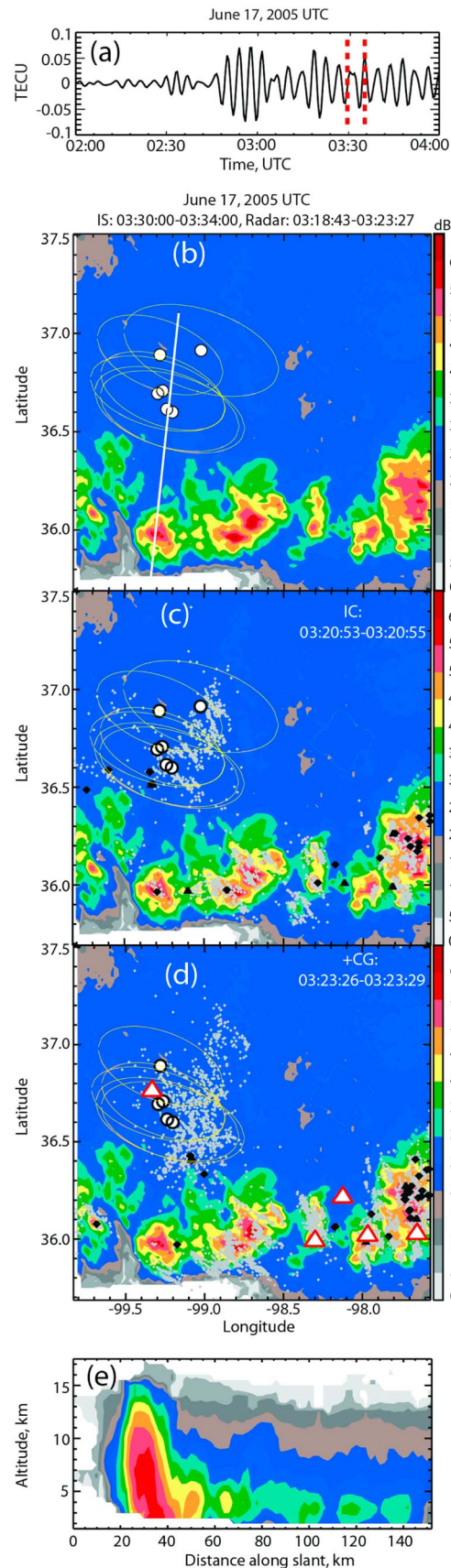
Figure 6. Same as Figure 5 but for another tornadic storm. (a) TEC oscillations. (b) Horizontal overlay. (c–h) Sequence of vertical cross sections from left to right through the black line in Figure 6b. The time for the infrasound sources is expected to be between the times of Figures 6g and 6h, while the precipitation core is descending, similar to that of Figures 4 and 5.



of the ionospheric oscillations. The infrasound sources are related to the storm stage between Figures 5g and 5h (22:48–23:00) when the precipitation core starts to descend, similar to that of the small storm in Figure 4. These comparisons of infrasound sources with storm development appears to suggest that ionospheric infrasound oscillations are more likely related to the storm downdraft than to the updraft or the tornado.

Figure 6 presents another example of supercell-related infrasound observations. Figure 6a is a replica of the black curve in Figure 1b to show the TEC variations related to this storm (between the red dashed lines), and Figure 6b is a replica of Figure 3b to compare with the storm's vertical development (Figures 6c–6h). The leftmost storm cell in Figure 6b spawned a tornado, at about 23:25 UTC and near $(-100.1^\circ, 36.9^\circ)$ at the south edge of the cell, as marked by the white square (http://www.spc.noaa.gov/climo/reports/050616_rpts.html). The infrasound sources related to this cell appear to surround the core of the cell along the 55 dBZ reflectivity contour. The rest of the sources appear to follow the cloud edge of the other cell just behind the tornadic cell. Figures 6c–6h show the time sequence of vertical cross sections of these two adjacent cells prior to and near the time of ionospheric oscillation (23:25–23:45 UTC; Figure 6a). The black line in Figure 6b shows the horizontal location of this vertical slice. Similar to that presented in Figure 5, the tornadic cell has an intense vertical development and its top reached above 18 km well over 30 min before the related oscillations were detected (Figures 6c–6f). Accounting for the infrasound propagation time (10–15 min), the sources are expected to occur at the times of Figures 6g and 6h when the storm's main precipitation core starts to descend, at the same storm stage as in Figures 4 and 5. The cell to the right in Figure 6 also reached over 18 km altitude long before the detection of the infrasonic oscillation, and its main precipitation core started to descend at about the same time as that of the left cell (Figures 6g and 6h). The sources that are related to this cell are located at the south edge of the cell (Figure 6b). Although it is not clear what storm process would be responsible for these sources, it has

Figure 7. Comparison of infrasound sources with radar and lightning observations in the stratiform region behind the mesoscale storm. (a) TEC oscillation record. Sources for this comparison occurred between the red dashed lines. (b) Radar reflectivity and source positions. (c and d) Overlay two extensive +CGs that occurred at the estimated infrasound source time. The red triangles show the ground-stroke locations for the +CGs, and the gray dots show the corresponding discharges inside the stratiform cloud. (e) The vertical cross section from left to right through the white line in Figure 7b.



been observed that downdraft commonly occurs at the edge of the cloud, the so-called “cloud-edge downdraft” [e.g., Knupp and Cotton, 1985; Knupp, 1987; Detwiler and Heymsfield, 1987].

4.2. Infrasonic Sources in Thunderstorm's Stratiform Regions

Although infrasound sources are expected to be related to the dynamically active regions of thunderstorms, we also often locate the sources in the stratiform regions of mesoscale and supercell storms. Figure 7 shows such an observation. This is the same mesoscale thunderstorm system on 4 June 2005 that contains the tornadic supercell discussed earlier in Figure 5. Here we examine the infrasonic TEC oscillations that occurred later in time between the red dashed lines in Figure 7a. Figure 7b overlays the located infrasound sources on a horizontal cross section of the mesoscale system at 7 km altitude. The radar reflectivity is chosen 10–15 min before the start of this oscillation burst (23:40–23:45 UTC). As shown in Figures 7b and 7e (a vertical cross section through the white line in Figure 7b), an extensive stratiform region, greater than 100×100 km in area, had developed behind the line of convective cells at this stage of the mesoscale storm, and the related infrasound sources are located in this region.

The stratiform region typically has little convective activity, although some moderate precipitation-related downdrafts can occur in some parts of the region. On the other hand, horizontally extensive, large-magnitude lightning discharges are observed frequently in this region, either within the cloud as intracloud (IC) lightning discharges or to the ground as cloud-to-ground (CG) discharges. Figures 7c and 7d overlay two positive CGs (+CG) that occurred between 23:42 to 23:44, about 10 min before the start of the related infrasonic oscillations. Positive CGs transport positive charge from cloud to ground and are a dominant type of lightning discharge in the stratiform regions of mesoscale, supercell, and severe storms. The red triangles indicate the ground-stroke locations of the two +CGs detected by the National Lightning Detection Network (NLDN) [Cummins et al., 1998], and the gray dots show the corresponding in-cloud source locations located by the OK-LMA (<http://www.nssl.noaa.gov/tools/oklma/>) [Rison et al., 1999]. Each +CG lasts about 1–2 s, and the peak current for both of the ground strokes is greater than

Figure 8. (a–e) Same as Figure 7 but for a different storm (7 June 2005). In Figure 8c gray dots show an extensive in-cloud discharge. Not ground stroke was detected for this discharge.

70 kA. The horizontal extent and the magnitude of the ground-stroke peak current suggest that each +CG would be capable of initiating mesospheric sprites discharges atop the lightning discharge regions [Cummer and Lyons, 2005]. Sprites are electric discharges extending from the bottom of the ionosphere (~90 km altitude) to the top of the thunderstorm [Sentman *et al.*, 1995] and are triggered by strong electric field disturbances generated by the underlying lightning discharges in large stratiform regions [e.g., Pasko *et al.*, 1996; Lyons *et al.*, 2008]. The good location coincidence between the infrasonic sources and the lightning discharge regions hints that the ionospheric oscillations could be related to the underlying lightning discharges or the consequent sprites atop the lightning discharges.

Figure 8 shows a similar observation of a mesoscale storm on 17 June 2005. The infrasonic sources are associated with ionospheric oscillations between 03:30 and 03:34 UTC (between the red dashed lines in Figure 8a) and are located in the stratiform region (Figure 8b). Sources for an extensive IC and an extensive and intense +CG (>70 kA peak current) that occurred at 03:20:53 and 03:23:26 are overlaid in Figures 8c and 8d. Similar to the previous case, the infrasonic source locations are coincident with the lightning discharge areas, suggesting the ionospheric oscillations might be related to the lightning discharges or to the consequent sprites.

Figures 8c and 8d also show numerous lightning discharges in the convective cells in the lower portion of the plots. However, these lightning discharges are much smaller in horizontal extent and are not likely to initiate sprites discharges.

Likewise in Figure 3a, the infrasound sources are similarly located in the stratiform region behind the supercell. In this case, three intense +CGs were reported (red triangles) on the backside of the cell during the estimated infrasonic source time period. Unfortunately, since this storm is too far from OK-LMA, no in-cloud lightning sources were located. Nevertheless, +CGs in such a storm commonly propagate away from the ground-stroke point into the stratiform region and discharge a great portion of the stratiform region, as shown in Figures 7c and 7d. Therefore, it is reasonable to infer that some or the combination of the three +CGs discharged the region where the infrasound sources were located, similar to the cases in Figures 7 and 8.

The observations in Figures 7, 8, and 3a suggest that in addition to the dynamic processes in the storm, extensive lightning discharges and their consequent mesospheric discharges (sprites) could be related to the infrasonic oscillations in the ionosphere. Lightning discharges produce acoustic signals in the audible frequencies (peaked around 50 Hz) [e.g., Holmes *et al.*, 1971] and in the infrasonic frequencies (a few tenths to a few hertz) [e.g., Holmes *et al.*, 1971; Few, 1985; Chum *et al.*, 2013]. The audible frequency signals are produced by abrupt heating and expansion of the lightning channels, and the infrasound signals are believed to be produced by the lightning-induced change in electrostatic field that leads to a sudden pressure change in the charged regions in the cloud. The concept of infrasound induced by the electrostatic effect was first introduced by Wilson [1920] and was later developed analytically by Dessler [1973] and others [e.g., Few, 1985; Pasko, 2009]. With typical charge structures and spatial scales in a thunderstorm, Dessler predicted that the infrasound signals would be radiated at frequencies between 0.2 and 2 Hz, as observed by Holmes *et al.* [1971] and later by Farges and Blanc [2010] and Chum *et al.* [2013] with ground-based microbarometers. In addition, infrasound signals in the frequency range of 0.1–10 Hz have been recently observed from sprites with similar ground-based sensors [Farges *et al.*, 2005; Farges and Blanc, 2010].

Due to background noise (wind), it is difficult to detect infrasound signals below 0.01 Hz on the ground, and therefore, it is difficult to compare the existent ground observations with the 3–5 min (3–5 mHz) ionospheric oscillations presented in this paper. Nevertheless, it is possible that lightning and sprites radiate over a broader frequency spectrum that spreads down to the mHz range and are responsible for ionospheric oscillations. Signals at higher frequencies (e.g., greater than 10 mHz) would be significantly attenuated at the lower boundary of the ionosphere due to the sharp increase of temperature at the lower boundary [Walterscheid *et al.*, 2003], and therefore cannot be detected in the ionosphere. Because of these different ranges of sensitivity, ground and ionospheric observations are complementary in frequency for infrasound detection.

Nevertheless, it is also possible that the ionospheric oscillations in Figures 7, 8, and 3a are solely related to the inferred sprites discharges atop the stratiform regions. Sprites can extend 40–70 km downward from the bottom of the ionosphere, and in cases of horizontally extensive +CGs, multiple sprites are commonly triggered by the same lightning discharge. These sprites occur laterally in the mesosphere, following the horizontal

development of the underlying lightning channels (private communication with Dr. Mark Stanley). Such a sprite system would discharge a large volume of the mesosphere in the scale of tens of kilometer along each side of the volume. Using $L = 60$ km for the 1-D scale and a characteristic time period calculation based on Dessler [1973], the characteristic infrasound time period produced by the electrostatic effect induced by the sprites would be $L/v = 60 \times 10^3/300 = 200$ s, where v is the sound speed in the mesosphere. This inferred infrasound time period is in a surprisingly good agreement with the oscillation period observed in the ionosphere, suggesting that sprites could be the source for the ionospheric infrasonic oscillation.

5. Discussion

In this paper, we present a new technique that locates the source of ionospheric infrasound oscillations by using an array of ground-based GPS-TEC measurements. The technique uses the instantaneous phase differences between pairs of spatially separated TEC measurements and a least χ^2 fit to best fit the phase-difference measurements with assumed source position, source height, and the effective infrasound propagation speed. We discussed the variances associated with the four fitted source parameters and the co-variances between the six pairs of the four parameters, and discussed their implications on the best fitted parameters. It is found that the source height estimated by this technique can only be treated as a virtual height, and the propagation speed can only be considered as an “effective” speed due to the nature of the infrasound propagation from troposphere to the ionosphere and the simple geometric raypath assumption for infrasound wave propagation. However, it is found that the horizontal source position is less sensitive to the height and speed and can be trusted if a good χ^2 fit is archived and other additional criteria are met.

This paper reports the first attempt to use the instantaneous phase difference in infrasonic TEC oscillations to locate the responsive sources, and the technique can be improved in many aspects. We note that several factors affect the location accuracy and the usefulness of this technique: (1) the signal strength, (2) the number of the GPS-TEC measurements, (3) the geometry of the baselines formed by the IPPs as relative to the source location, and (4) the phase accuracy of the measurement. Among these, the phase accuracy can be improved by using the GPS-TEC data that are sampled at 1 s time interval instead of the now 30 s interval. The finer sampling is available in recent TEC measurements for many operating GPS receivers, but the data are not archived regularly for later analyses. Another limitation in this preliminary study is the assumption of a single source at each time instant (every 30 s), which will not result in a good geolocation if multiple, interfering sources are present at the same time. For instance, some of the oscillations in Figure 1c (around 23:00) and Figure 5a (around 23:40) were not located by the current approach. However, with enough spatially separated GPS-TEC measurements, it would be possible to “image” multiple sources at the same time. Further development is needed to achieve this capability.

In this study, we assume that the infrasound signal propagates along geometric raypaths from the source to the IPPs and that is part of the reason for our best fitted source height being unphysical in many cases, even though the 2-D source position appears not being affected. In the future, we plan to implement a more realistic ray-tracing calculation in our approach that will take into account of the infrasound velocity profile and the wind field profile from the ground to the ionosphere. To do so, we will need to consider the entire region and depth of the *disturbed* ionosphere to include the integrated TEC variation effect along the line of sight from the GPS receiver to the satellite, to assure its accuracy. This more accurate approach will require more extensive computation but should be feasible.

Using this location technique, we have examined 5 days of infrasonic TEC measurements over the Great Plains when severe thunderstorms occurred in the area. We find that the sources are often located near the storms’ core region, but they are equally often located in the storms’ stratiform region. In this paper we compared the infrasound sources in time and space with the thunderstorms’ vertical development and the stratiform-region lightning discharges for a few selected cases. For sources near the core region, we found that the sources are more likely related to the downdraft than to the updraft process in the storm. This is specifically supported by the analysis of the small, isolated storm in Figure 4, where the sources are coincident in time and space with an inferred midlevel downdraft at the mature stage of the storm but are not coincident with the upward development at the cumulus stage. Observations of the more complicated supercell, tornadic storms in Figures 5 and 6 appear to be consistent with those of the small storm in terms of the relation between source time and location and the development of the cells. Nevertheless, it is not clear

to the authors why the 3–5 min period infrasound appears to be preferably related to the downdraft than to the updraft. Furthermore, with the location uncertainty and the limited analysis, we cannot rule out other processes near the storm core that might be responsible for the infrasound oscillations.

Since the storms' stratiform region is typically quiet in convection, we compared the infrasound sources in this region with the common horizontally extensive and intense lightning discharges (Figures 7, 8, and 3a). The good correlation between infrasound source and lightning discharges suggests that the corresponding ionospheric oscillations could be related to lightning discharges in this region. Furthermore, extensive lightning discharges (either +CG or in-cloud discharge) in this region are known to commonly initiate sprites (high-altitude mesospheric discharges). Based on Dessler's [1973] electrostatic theory and given the spatial scale of the sprites, it is found that sprites would produce the infrasound oscillations at the same frequency range (3–5 mHz) as those detected in the ionosphere, and therefore, sprite discharges are more likely to be the sources for such oscillations than lightning itself.

Acknowledgments

We thank Timothy Hamlin for the preparation of OK-LMA lightning data and Kyle Wiens for the display tools for NEXRAD observations. This research was supported by the Los Alamos National Laboratory's Laboratory Directed Research and Development and Institute for Geophysics, Planetary Physics and Signatures offices. Ground-based GPS receiver data used in this study were downloaded from <http://geodesy.noaa.gov/CORS/>. NEXRAD radar data were downloaded from <http://www.roc.noaa.gov/WSR88D/>.

References

- Baker, D. M., and K. Davies (1969), F2-region acoustic waves from severe weather, *J. Atmos. Terr. Phys.*, **31**, 1345–1352.
- Bevington, P. R., and D. K. Robinson (1992), *Data Reduction and Error Analysis for the Physical Sciences*, McGraw-Hill, New York.
- Burrell, A. G., N. A. Bonito, and C. S. Carrano (2009), Total electron content processing from GPS observations to facilitate ionospheric modeling, *GPS Solutions*, **13**(2), doi:10.1007/s10291-008-0102-3.
- Chum, J., G. Diendorfer, T. Šindelářová, J. Baše, and F. Hruška (2013), Infrasound pulses from lightning and electrostatic field changes: Observation and discussion, *J. Geophys. Res. Atmos.*, **118**, 10,653–10,664, doi:10.1002/jgrd.50805.
- Cummer, S. A., and W. A. Lyons (2005), Implications of impulse charge moment changes in sprite-producing and non-sprite producing lightning, *J. Geophys. Res.*, **110**, A04304, doi:10.1029/2004JA010812.
- Cummins, K. L., M. J. Murphy, E. A. Bardo, W. L. Hiscox, R. B. Pyle, and A. E. Pifer (1998), A combined TOA/MDF technology upgrade of the U.S. National Lightning Detection Network, *J. Geophys. Res.*, **103**(D8), 9035–9044, doi:10.1029/98JD00153.
- Davies, K., and J. E. Jones (1971), Ionospheric disturbances in the F2 region associated with severe thunderstorms, *J. Atmos. Sci.*, **28**, 254–262.
- Davies, K., and J. E. Jones (1973), Acoustic waves in the ionospheric F2-region produced by severe thunderstorm, *J. Atmos. Terr. Phys.*, **35**, 1737–1744.
- Dessler, A. J. (1973), Infrasonic thunder, *J. Geophys. Res.*, **78**, 1889–1896, doi:10.1029/JC078i012p01889.
- Detweiler, A., and A. J. Heymsfield (1987), Air motion characteristics in the Anvil of a severe thunderstorm during CCOPE, *J. Atmos. Sci.*, **44**, 1899–1911.
- Drob, D. P., et al. (2008), An empirical model of the Earth's horizontal wind fields: HWM07, *J. Geophys. Res.*, **113**, A12304, doi:10.1029/2008JA013668.
- Farges, T., and E. Blanc (2010), Characteristics of infrasound from lightning and sprites near thunderstorm areas, *J. Geophys. Res.*, **115**, A00E31, doi:10.1029/2009JA014700.
- Farges, T., E. Blanc, A. Le Pichon, T. Neubert, and T. H. Allin (2005), Identification of infrasound produced by sprites during the Sprite2003 campaign, *Geophys. Res. Lett.*, **32**, L01813, doi:10.1029/2004GL021212.
- Few, A. A. (1985), The production of lightning-associated infrasonic acoustic sources in thunderclouds, *J. Geophys. Res.*, **90**, 6175–6180, doi:10.1029/JD090iD04p06175.
- Georges, T. M. (1968), HF Doppler studies of traveling ionospheric disturbances, *J. Atmos. Terr. Phys.*, **30**, 735–746.
- Georges, T. M. (1973), Infrasound from convective storms: Examining the evidence, *Rev. Geophys. Space Phys.*, **11**, 571–594.
- Georges, T. M., and W. H. Hooke (1970), Wave-induced fluctuations in ionospheric electron content: A model indicating some observational biases, *J. Geophys. Res.*, **75**(31), 6295–6308, doi:10.1029/JA075i031p06295.
- Gómez, D., et al. (2015), Virtual array beamforming of GPS TEC observations of coseismic ionospheric disturbances near the Geomagnetic South Pole triggered by teleseismic megathrusts, *J. Geophys. Res. Space Physics*, **120**, 9087–9101, doi:10.1002/2015JA021725.
- Holmes, C. R., M. Brook, P. Krehbiel, and R. McCrory (1971), On the power spectrum and mechanism of thunder, *J. Geophys. Res.*, **76**, 2106–2115, doi:10.1029/JC076i009p02106.
- Kingsmill, D. E., and R. M. Wakimoto (1991), Kinematic, dynamic, and thermodynamic analysis of a weakly sheared severe thunderstorm over northern Alabama, *Mon. Weather Rev.*, **119**, 262–297.
- Knupp, K. R. (1987), Downdrafts within high plains cumulonimbi Part II: Dynamics and thermodynamics, *J. Atmos. Sci.*, **44**, 987–1008.
- Knupp, K. R., and W. R. Cotton (1985), Convective cloud downdraft structure: An interpretative survey, *Rev. Geophys.*, **23**, 183–215, doi:10.1029/RG023i002p00183.
- Lay, E. H., X.-M. Shao, and C. S. Carrano (2013), Variation in total electron content above large thunderstorms, *Geophys. Res. Lett.*, **40**, 1945–1949, doi:10.1002/grl.50499.
- Lay, E. H., X.-M. Shao, A. K. Kendrick, and C. S. Carrano (2015), Ionospheric acoustic and gravity waves associated with midlatitude thunderstorms, *J. Geophys. Res. Space Physics*, **120**, 6010–6020, doi:10.1002/2015JA021334.
- Lemon, L. R., and C. A. Doswell (1979), Severe thunderstorm evolution and mesocyclone structure as related to tornadogenesis, *Mon. Weather Rev.*, **107**, 1184–1197.
- Lyons, W. A., S. A. Cummer, M. A. Stanley, G. R. Huffines, K. C. Wiens, and T. E. Nelson (2008), Supercells and sprites, *Bull. Am. Meteorol. Soc.*, **89**, 1165–1174, doi:10.1175/2008BAMS2439.1.
- Marshall, R. A., and J. B. Snively (2014), Very low frequency subionospheric remote sensing of thunderstorm-driven acoustic waves in the lower ionosphere, *J. Geophys. Res. Atmos.*, **119**, 5037–5045, doi:10.1002/2014JD021594.
- Nishioka, M., T. Tsugawa, M. Kubota, and M. Ishii (2013), Concentric waves and short-period oscillations observed in the ionosphere after the 2013 Moore EF5 tornado, *Geophys. Res. Lett.*, **40**, 5581–5586, doi:10.1002/2013GL057963.
- Oppenheim, A. V., and R. W. Schaffer (1999), *Discrete-Time Signal Processing*, 2nd ed., Prentice-Hall, Inc., New Jersey.
- Park, J., R. B. von Frese, D. A. Grejner-Brzezinska, Y. Morton, and L. R. Gaya-Pique (2011), Ionospheric detection of the 25 May 2009 North Korean underground nuclear test, *Geophys. Res. Lett.*, **38**, L22802, doi:10.1029/2011GL049430.

- Pasko, V. P. (2009), Mechanism of lightning-associated infrasonic pulses from thunderclouds, *J. Geophys. Res.*, *114*, D08205, doi:10.1029/2008JD11145.
- Pasko, V. P., U. S. Inan, and T. F. Bell (1996), Sprites as luminous columns of ionization produced by quasioleostatic thundercloud fields, *Geophys. Res. Lett.*, *23*, 649–652, doi:10.1029/96GL00473.
- Pilger, C., C. Schmidt, F. Streicher, S. Wüst, and M. Bittner (2013), Airglow observations of orographic, volcanic and meteorological infrasound signatures, *J. Atmos. Sol. Terr. Phys.*, *104*, 55–66.
- Prasad, S. S., L. J. Schneck, and K. Davies (1975), Ionospheric disturbances by severe tropospheric weather storms, *J. Atmos. Terr. Phys.*, *37*, 1357–1363.
- Raju, D. G. K., M. S. Rao, B. M. Rao, C. Jogulu, C. P. Rao, and R. Ramanadham (1981), Infrasonic oscillations in the F_2 region associated with severe thunderstorms, *J. Geophys. Res.*, *86*(A7), 5873–5880, doi:10.1029/JA086iA07p05873.
- Rison, W., R. J. Thomas, P. R. Krehbiel, T. Hamlin, and J. Harlin (1999), A GPS-based three-dimensional lightning mapping system: Initial observations in central New Mexico, *Geophys. Res. Lett.*, *26*, 3573–3576, doi:10.1029/1999GL010856.
- Seemala, G. K., and C. E. Valladares (2011), Statistics of total electron content depletions observed over the South American continent for the year 2008, *Radio Sci.*, *46*, RS5019, doi:10.1029/2011RS004722.
- Sentman, D. D., E. M. Wescott, D. L. Osborne, D. L. Hampton, and M. J. Heavner (1995), Preliminary results from the Sprites94 aircraft campaign: 1. Red sprites, *Geophys. Res. Lett.*, *22*, 1205–1208, doi:10.1029/95GL00583.
- Sindelarova, T., D. Buresova, J. Chum, and F. Hruska (2009), Doppler observations of infrasonic waves of meteorological origin at ionospheric heights, *Adv. Space Res.*, *43*, 1644–1651.
- Snively, J. B. (2013), Mesospheric hydroxyl airglow signatures of acoustic and gravity waves generated by transient tropospheric forcing, *Geophys. Res. Lett.*, *40*, 4533–4537, doi:10.1002/grl.50886.
- Thompson, A. R., J. M. Moran, and G. W. Swenson (2001), *Interferometry and Synthesis in Radio Astronomy*, 2nd ed., John Wiley, New York.
- Walterscheid, R. L., G. Schubert, and D. G. Brinkman (2003), Acoustic waves in the upper mesosphere and lower thermosphere generated by deep tropical convection, *J. Geophys. Res.*, *108*(A11), 1392, doi:10.1029/2003JA010065.
- Wilson, C. T. R. (1920), Investigations on lightning discharges and on the electric field of thunderstorms, *Philos. Trans. R. Soc., A*, *221*, 73–115.
- Zettergren, M. D., and J. B. Snively (2013), Ionospheric signatures of acoustic waves generated by transient tropospheric forcing, *Geophys. Res. Lett.*, *40*, 5345–5349, doi:10.1002/2013GL058018.
- Zettergren, M. D., and J. B. Snively (2015), Ionospheric response to infrasonic-acoustic waves generated by natural hazard events, *J. Geophys. Res. Space Physics*, *120*, 8002–8024, doi:10.1002/2015JA022116.